ADVANCED MATERIALS TECHNOLOGIES
www.advmattechnol.de

High-Resolution Kinoform X-Ray Optics Printed via 405 nm 3D Laser Lithography

Umut T. Sanli, Tobias Messer,* Markus Weigand, Lars Lötgering, Gisela Schütz, Martin Wegener, Christian Kern, and Kahraman Keskinbora**

Efficient focusing of X-rays is essential for high-resolution X-ray microscopy. Diffractive X-ray optics called kinoforms offer the highest focusing efficiencies in theory. However, they have long remained unavailable due to their challenging nanofabrication. Recently, various X-ray optic geometries including kinoforms have been realized using 3D laser lithography at near-infrared wavelengths. As the smallest features (period) of the kinoform determines the resolving power, there is a natural drive to find ways to fabricate kinoforms with ever smaller features. Here, a custom-built 3D laser lithography setup with an excitation wavelength of 405 nm is used, which allows to half the smallest period of the kinoforms compared to previous work. A 40% improvement in scanning transmission X-ray microscopy image resolution, that is, a cutoff resolution of 145 nm, and an efficiency of 7.6% at 700 eV is achieved. A reconstructed pixel size of 18.5 nm, reaching the limit imposed by the design of the microscopy set-up, is demonstrated through ptychographic imaging of a magnetic sample which has a strongly reduced contrast mechanism. Moreover, X-ray lenses manufactured by 405 nm 3D laser lithography have the potential to become much less expensive than X-ray lenses made by other means.

1. Introduction

After his discovery of X-rays in 1985, Röntgen describes an image of a human hand and the shadows cast by the bones, thereby demonstrating a novel nondestructive technique to visualize hidden objects. In the following decades, X-ray microscopy emerged[1,2] and with the advent of highly-brilliant synchrotron sources, about 70 years after Röntgen's discovery, evolved into an essential tool for the natural sciences.[3,4] Today, X-ray microscopy is used for a diverse field of applications from single-cell imaging[5,6] to microstructure analysis and tomography,[7] and supports a wide range of research fields from materials science to the semiconductor industry.[8,9] To further advance X-ray microscopy, multi-billion investments are being made in new X-ray sources with yet higher brilliance and coherence, such as free electron lasers and fourth generation synchrotrons.[10]

Following Abbe's criterion, the achievable resolution in diffraction limited optical systems fundamentally scales with the wavelength of the radiation used. Thus, a few orders of magnitude better resolution can be achieved by using X-rays instead of visible light. However, the superior resolution comes at a price. In the X-ray regime, the real part of the refractive index of most materials is very close to one. Consequently, single refractive lenses with high numerical apertures are not available for X-ray microscopy. Instead, so-called Fresnel zone plates (FZPs), which rely on diffraction rather than refraction,

U. T. Sanli, G. Schütz, K. Keskinbora
Modern Magnetic Systems Department
Max Planck Institute for Intelligent Systems
70569 Stuttgart, Germany
E-mail: sanli@is.mpg.de; kahraman@mit.edu

T. Messer, M. Wegener, C. Kern
Institute of Applied Physics
Karlsruhe Institute of Technology (KIT)
76128 Karlsruhe, Germany
E-mail: tobias.messer@kit.edu

The ORCID identification number(s) for the author(s) of this article can be found under https://doi.org/10.1002/admt.202101695.

DOI: 10.1002/admt.202101695

M. Weigand
Helmholtz-Zentrum Berlin für Materialien und Energie GmbH
12489 Berlin, Germany

L. Lötgering
Institute of Applied Physics and Abbe Center of Photonics
Friedrich-Schiller-University Jena
Albert-Einstein-Straße 15, 07745 Jena, Germany

L. Lötgering
Helmholtz-Institute Jena
Fröbelstieg 3, 07743 Jena, Germany

L. Lötgering
Leibniz Institute of Photonic Technology
Albert-Einstein-Straße 9, 07745 Jena, Germany

M. Wegener, C. Kern
Institute of Nanotechnology
Karlsruhe Institute of Technology (KIT)
76021 Karlsruhe, Germany

K. Keskinbora
Massachusetts Institute of Technology
77 Mass Avenue, Cambridge, MA 02139, USA

are extensively used.[11–17] The simplest version of FZPs, binary FZPs, consist of concentric annuli that alternate between fully transparent and opaque zones. A disadvantage of binary absoprtion FZPs lies in their limited focusing efficiencies of ~10% in theory.

Focusing efficiencies reaching 100% can be achieved in the theoretical lossless limit by correcting the intra-period optical path-length difference of a FZP for every zone[18] by introducing a surface relief profile. Such special FZPs, which are called kinoforms, have been known since decades.[19,20] The correction of the intra-period optical path-length differences requires distinctive parabolic profile of the kinoforms. Moreover, in diffractive X-ray optics one often uses a central stop that blocks the nondiffracted light. This stop slightly improves the resolution, but makes the light go in the side lobes of the Airy disc. In ideal kinoforms, a central stop is neither needed nor wanted. It would only increase the energy going into the side lobes. However, the practical realization of X-ray kinoforms with their complex 3D nanoscale profiles and high aspect ratios is exceptionally challenging, despite the rapid advancement of modern fabrication techniques.[21–25]

Kinoforms are not only relevant for conventional X-ray microscopy: In the last decade, with the emergence of powerful X-ray CCD cameras, faster computing, and optimized reconstruction algorithms, various flavors of coherent imaging techniques such as ptychography have moved into the focus.[26,27] In a typical ptychography experiment, a sample is scanned with partly overlapping sample illumination while the diffraction patterns are recorded. An iterative reconstruction algorithm simultaneously reconstructs the complex object exit-wave and probe functions from these recorded intensities. In contrast to imaging using FZPs, ptychography provides a resolution much better than the focal spot size, theoretically limited by the wavelength of the incident X-rays. In practice, the resolution of the reconstructed image is limited by the largest detectable scattering angle, where the intensity drops sharply. As a consequence, the performance of ptychography depends on the brightness and the coherence of the illumination function. Hence, thanks to the decoupling of the achieved resolution and the resolving power of the optic, already an intermediate-resolution focusing optic with a sub-micron spot size with improved efficiency greatly benefits ptychography.[28] Consequently, kinoforms with sub-micrometer resolution and high diffraction efficiencies are not only attractive for medium-resolution scanning transmission X-ray microscopy (STXM) but also for high-performance X-ray ptychography.

Recently, the fabrication of high-quality kinoforms has been demonstrated using conventional 3D laser lithography at an excitation wavelength of 780 nm.[29] In this paper, we show the merit of a reduction of the excitation wavelength to 405 nm using a custom-built 3D laser lithography setup for the advanced fabrication of X-ray kinoforms. Using these kinoforms as the lens of a state-of-the-art STXM, we evaluate their performance in both STXM and ptychography experiments, demonstrating an improvement in focal spot size and resolution by a factor of about two as compared to the aforementioned previous results[29] and a 7.6% efficiency at 700 eV X-ray energy. Our work paves the way for a fast and cost-efficient fabrication of high-resolution 3D kinoforms and reinforces the trend toward shorter excitation wavelengths in 3D laser lithography.

2. Results and Discussion

2.1. 3D Laser Lithography

The most commonly used version of 3D laser lithography employs a femtosecond-pulsed near-infrared laser which is tightly focused into a reservoir of liquid negative-tone photoresist. In a small volume of the laser focus, a so-called voxel, the resist is sufficiently crosslinked to withstand the subsequent development process. Scanning the laser focus using a galvanometer mirror system or moving the photoresist reservoir with respect to the laser focus allows for the fabrication of almost arbitrary 3D structures with sub-micrometer resolution.

The performance of kinoforms is directly linked to the resolution of the manufacturing process. While the resolution of 3D laser lithography is much higher than that of most other 3D printing techniques,[30] it is fundamentally limited by diffraction—provided that the photoresist is not limiting the spatial resolution. Under these conditions, the minimum distance between two neighboring point exposures is determined by the two-photon Sparrow criterion, which can be approximated by the two-photon modified Abbe criterion[31]

$$d_{\min} = \frac{\lambda}{2\sqrt{2}\mathrm{NA}} \tag{1}$$

where λ is the excitation wavelength in free space and NA is the numerical aperture of the objective lens.

Using high-NA objective lenses, two possibilities of obtaining higher resolution remain. First, one can overcome the diffraction limit by, for example, adapting the idea of stimulated-emission-depletion (STED).[31] Using this approach, line gratings with periods below 200 nm were achieved.[32,33] However, STED requires complex setups and special resist systems. Second, and more obvious, following the decade-long trend of the semiconductor industry, one can decrease the wavelength used for excitation. Here, we employ a reduction of the excitation wavelength from the conventionally used region around 800 to 405 nm. This enabled us to roughly halve the outermost period of the kinoforms as compared to the aforementioned previous work,[29] which directly translates to a doubled cutoff resolution of the lens in theory.

This wavelength reduction requires a change of the photoresist composition. Typically, the photoresist consists of two main components: a monomer, which can crosslink via a radical polymerization reaction to form dense polymer networks, and a photoinitiator, which is nonlinearly excited by the laser in the visible or near-infrared regime and triggers the polymerization reaction. By reducing the wavelength to 405 nm, the radical polymerization reaction can be triggered by directly nonlinearly exciting the monomer itself without the need for a dedicated photoinitiator.[34] An example of a suitable resist is pure pentaerythritol triacrylate (PETA), an acrylatic monomer that is frequently used in 3D laser lithography.

Fabrication of the kinoforms was carried out using a home-built 3D laser lithography setup[35] which shares its basic design with many commercially available setups while offering additional flexibility (see Experimental Section for a detailed description). The setup comprises a piezoelectric stage for

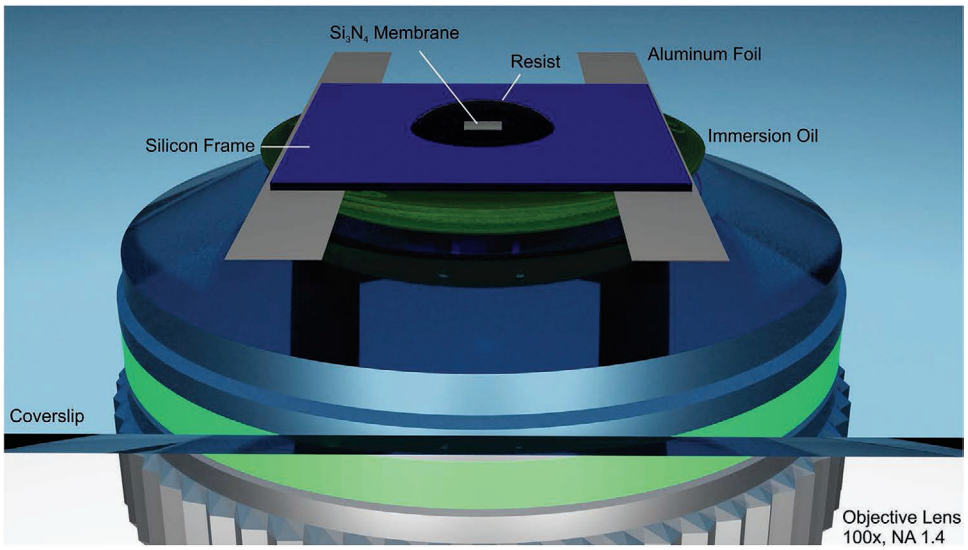

Figure 1. Scheme of the writing configuration. A substrate comprising a 100 nm thin silicon nitride membrane suspended by a 100 µm thick silicon frame is placed on top of a glass coverslip with small stripes of aluminum foil serving as spacers. The silicon nitride membrane faces the coverslip. Femtosecond light pulses with a center wavelength of 405 nm are focused by using a high-NA oil-immersion objective lens through the coverslip and through the optically transparent silicon nitride membrane into the drop-cast liquid photoresist. Additional immersion oil between the coverslip and the substrate guarantees refractive-index matching.

moving the sample with respect to the laser focus along almost any desired 3D trajectory. Silicon nitride membranes embedded in silicon frames were used as substrates, enabling the characterization of the kinoforms in X-ray microscopy experiments. The targeted high-resolution and the constraints imposed by the working distance of the objective lens led to the intricate writing configuration shown in **Figure 1**.

3D models of the kinoforms were generated according to the usual set of parametric equations[36] (see Experimental Section for details). An illustration of the geometry is shown in **Figure 2**a. The outermost period, Λ, determines the resolution of the lens, while its thickness, t, is chosen such that the optical path difference, $\Delta\Phi$, is equal to 2π. The 3D models were then converted to sets of coordinates forming the trajectories for the piezoelectric stage and the kinoforms were printed. The quality of the structures was optimized by systematically varying both the writing speed and the excitation power. Scanning electron micrographs of the 3D printed structures are shown in Figure 2b,c.

2.2. X-Ray Focusing Performance

The kinoforms presented in this paper were designed for an X-ray energy of 700 eV. Being diffractive optics, such as zone plates, the kinoforms achieve their peak efficiency at the design photon energy. However, it is known that the diffraction efficiency stays very high in a range of several hundreds of eV around the design energy.[29] From the fabricated kinoforms, one was selected randomly to be tested at a state-of-the-art scanning transmission X-ray microscope, MAXYMUS (magnetic X-ray microscope with UHV spectroscopy), at the UE46-PGMII beamline of BESSY II. The experimental setup is shown in **Figure 3** (see ref. [37] for details).

The diffraction efficiency was tested by a pinhole scan method (see **Figure 4**a for an example and Experimental Section for a detailed explanation) in the photon energy range between 600 and 1100 eV (see Figure 4b). The kinoform demonstrated a reasonable diffraction efficiency throughout the tested energy range, achieving a peak diffraction efficiency of 7.6% at 700 eV

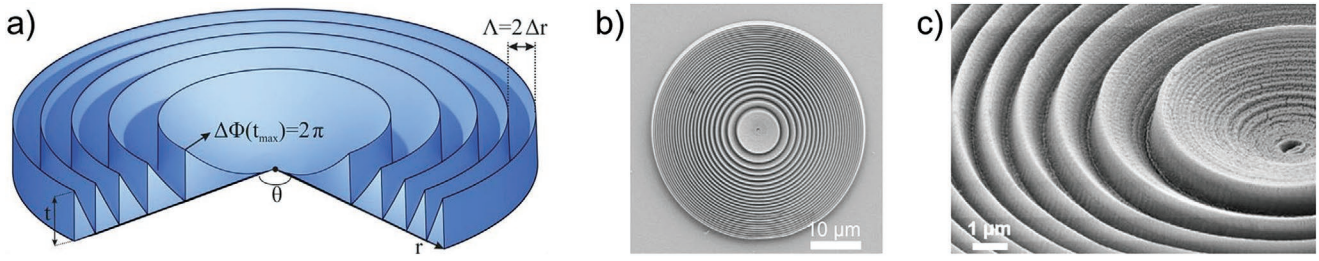

Figure 2. a) Schematic representation of a kinoform illustrating its distinctive parabolic surface profile and geometry parameters. Ideally, the optical path difference, $\Delta\Phi$, at maximum thickness, t_{max}, is equal to 2π. The resolution is determined by the outermost period, Λ, which is equivalent to two outermost zone widths (Δr) of an equivalent binary Fresnel zone plate. b,c) Scanning electron micrographs of a kinoform fabricated on a glass substrate, and its first few inner ridges in detail, respectively.

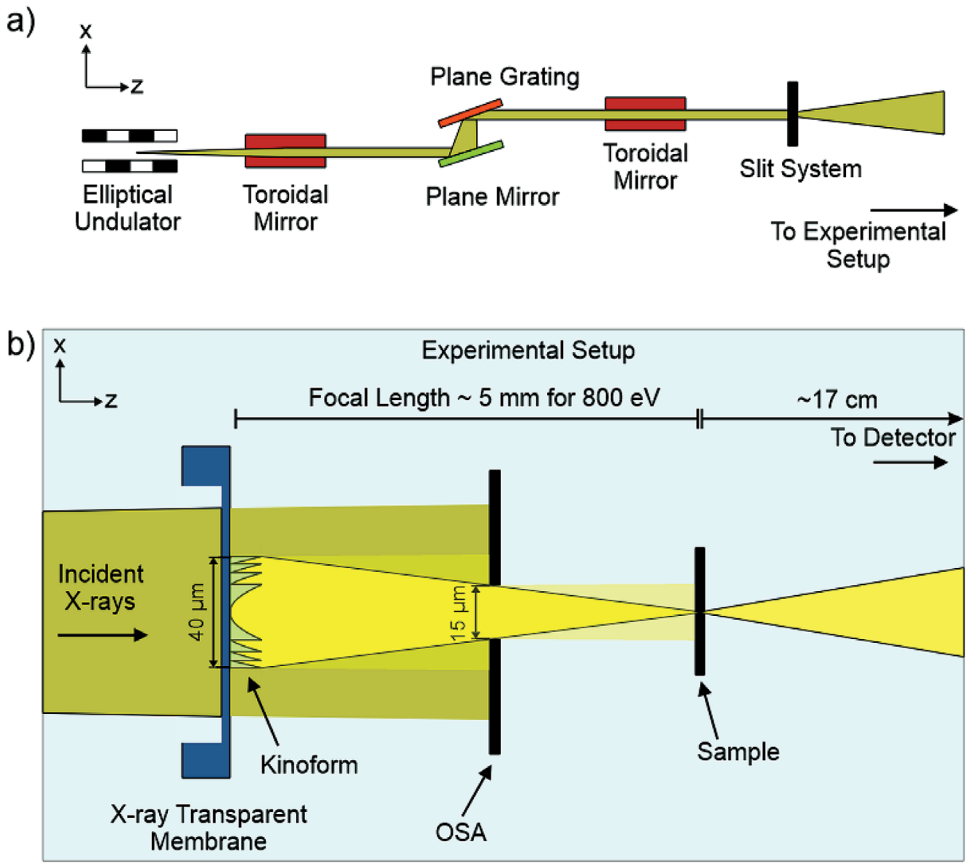

Figure 3. a) Schematic illustration of the undulator-based X-ray source and beamline optics. The electrons from the storage ring pass through an Apple-II type helical undulator and create energy and polarization tunable X-rays. After passing through a set of toroidal mirrors and plane grating monochromator filters, the X-rays are incident onto a set of slits. The slits act as a secondary source and determine the coherence on the optic located 3 m downstream. b) Illustration of the experimental setup of the MAXYMUS scanning transmission X-ray microscope. The kinoform optic that is fully coherently illuminated focuses the X-rays into a set of foci on the optical axis. An order selecting aperture (OSA) filters the spurious diffraction orders. The sample is located at the focal plane. An interferometrically controlled piezo scanner is used for raster scanning with nanometer level accuracy. An avalanche photodiode (APD) and a CCD can be used as the detector for STXM and ptychography experiments, respectively.

as depicted in Figure 4b. The reason for lower than ideal efficiencies are attributed to the printing errors and surface roughnesses which are visible in the SEM images. The roughness is not expected to change the resolution of the optic. The current kinoform design has half the outermost zone width (200 nm instead of 400 nm) and a slightly larger diameter (40 µm instead of 38 µm), compared to our previous work.[29] Confluent with an increase in the number of zones, the current kinoform offers a five times greater focal plane intensity, in theory. The reason for this impressive improvement is the quadratic dependence of the focal plane intensity on the number of zones, given by the following equation,[18]

$$\frac{I(\theta)}{I(0)} = N^2 \left| \frac{2J_1(k\alpha\theta)}{(k\alpha\theta)} \right|^2 \tag{2}$$

where $I(\theta)/I(0)$ is the relative focal plane intensity, N is the number of zones in an equivalent zone plate, J_1 is the Bessel function of first kind and first order, $k = 2\pi/\lambda$, a is the kinoform radius, and the function inside the brackets is the Airy pattern. A comparison of the theoretical radial intensity distributions of the Airy patterns for the current and previous kinoform designs in 1D is shown in the Figure 4c. Besides the five times greater focal plane intensity, the two times smaller focal spot size, which is due to the two times smaller outermost zone width, is also evident in the graph.

We assessed and cross-validated the STXM resolution and focal spot size of our kinoform using three independent methods. First, we performed STXM scans on a varying line space grating and determined the spatial frequencies at which the contrast disappears into the noise floor. An integrated intensity profile of the STXM image was used to determine the cutoff resolution. The half-pitch cutoff resolution was estimated to be 145 nm as depicted in **Figure 5**a. Second, a Siemens star test sample with 30 nm smallest features was imaged. The tips of the third inner ring, which correspond to a smallest feature-size of 120 nm, are barely not resolved (see Figure 5b), in general agreement with the linear test sample. The resolution of the linear and horizontal structures does not show a significant amount of astigmatism. Third, a Fourier ring correlation analysis with a 1/7 threshold was performed, which also reveals a 285 nm full-pitch cutoff resolution,

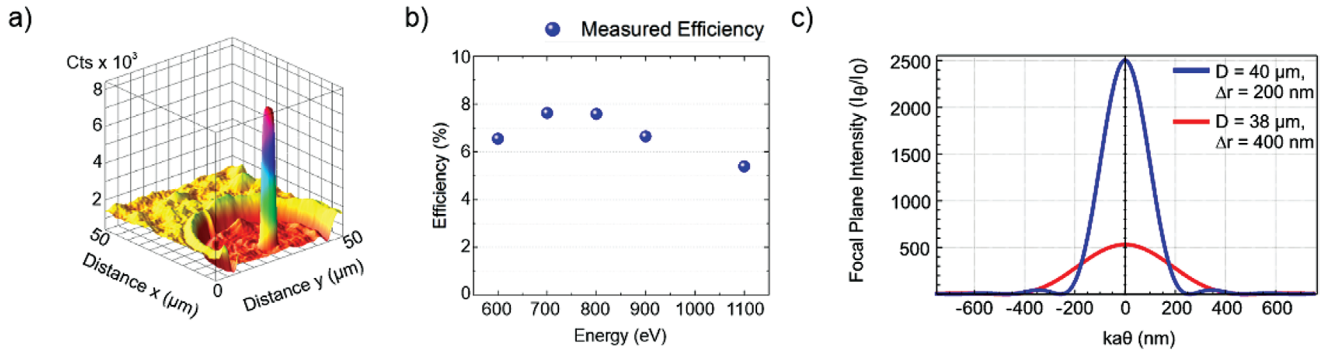

Figure 4. a) A 4.4 μm diameter pinhole was scanned in the focal plane to reveal the first order focal intensity, the incident intensity, and the zeroth order light (undiffracted light transmitted through the zones of the FZP). b) Measured efficiency of the kinoform at various photon energies. c) Comparison of the calculated focal plane intensity profiles of two different kinoform designs.

agreeing with the results mentioned above, as depicted in Figure 5c.

To evaluate the kinoform's zone quality, we imaged the kinoform as a sample at MAXYMUS in STXM using a second kinoform, with an identical design and fabrication parameters, as the focusing optic. The resulting image is shown in Figure 5d. Here, a nonconcentricity of the lens is visible, which is quantified by the distance between the center of the zones and the brightest pixel in the image corresponding to $\gamma = 385$ nm. This value is slightly larger than the tolerance values stated in the literature for our designed optic ($\gamma < 1.2\Delta r = 240$ nm).[38] The nonconcentricity is expected to cause a slight coma aberration.[38]

Furthermore, we deduced a map of the relative optical thickness, Δx, of the parabolic zones from the STXM image. Assuming a uniform volumetric mass density distribution, ρ, and a uniform mass absorption coefficient, μ, throughout the

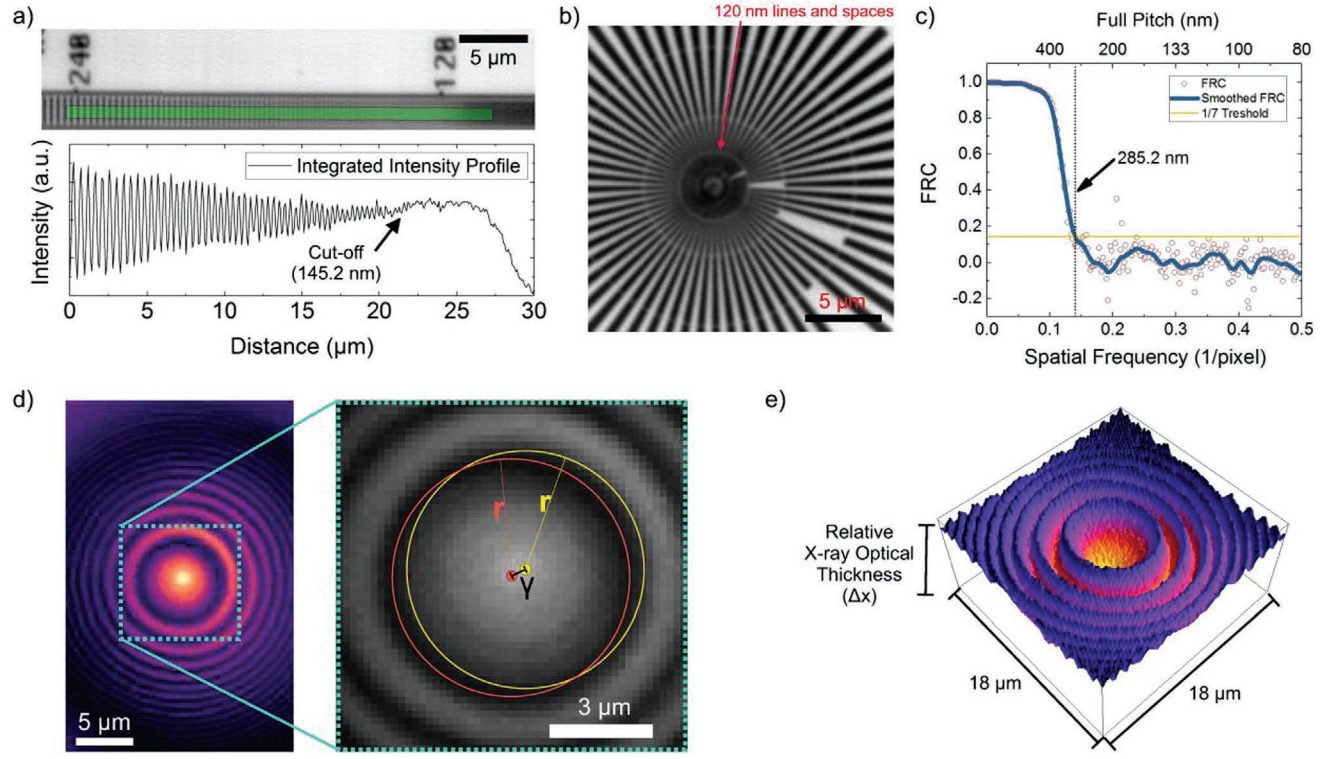

Figure 5. STXM imaging results. a) STXM image of a linear test sample consisting of gold strips with varying width and period (top) and integrated intensity profile of the green area of the linear test sample showing a cutoff resolution of 145.2 nm (bottom). b) STXM image of a Siemens star test sample. The second ring of the Siemens Star indicated with the red arrow corresponds to 120 nm lines and spaces, indicating the resolution to be slightly worse than 120 nm. c) Fourier ring correlation results obtained from two images of the Siemens Star acquired with the same scanning parameters. A 285.2 nm full pitch cutoff resolution (1/7 threshold) corresponding to a 147.6 nm half pitch resolution was achieved. d) STXM image of the kinoform imaged using a second, nominally identical kinoform (left) and the innermost zone (right) showing the amount of nonconcentricity $\gamma = 385$ nm e) Relative X-ray optical thickness of the kinoform deduced from the STXM image shown in (d).

kinoform, the relative thickness of the zones can be estimated by the Beer–Lambert law. To do so, we first took the natural logarithm of each pixel of the image in Figure 5d and then inverted the image using the open-source image processing software ImageJ.[39] A 3D surface plot of the resulting relative X-ray optical thickness distribution is shown in Figure 5e. This method is superior in characterizing X-ray optics to surface imaging techniques such as scanning electron microscopy in the sense that the X-ray absorption map gives the volume profile of the kinoform, which is important for the X-ray optical performance. Structural roughness inside the kinoform, density variations or porosity inside the zones can be visualized. However, due to the fact that we used a second kinoform as the focusing optic, only the innermost zones are accurately represented. Figure 5e shows a slight tilt in the inner zones of the kinoform. The relative optical thickness distribution of the kinoform gives no indication of substantial inhomogeneity in the volume of the printed kinoform.

The relatively low diffraction efficiencies shown in Figure 4b are at least partly attributed to the measured nonconcentricity of the kinoform, which is likely caused by a drift of the sample with respect to the laser focus during the fabrication process. Such a drift could also explain the slight tilt in the inner zones that can be seen in Figure 5e. As the effects of drifts are typically less pronounced for shorter fabrication times, one promising avenue to obtain higher efficiencies in future studies is the use of a galvanometer mirror system instead of a piezoelectric stage in the printer set-up. Such a system could reduce the fabrication time from about 3 h down to several minutes or even less.

Because the performance of ptychography has been linked to the available dose incident on the sample,[28] we define the figure-of-merit of a kinoform as the dose in its focal spot. Using this figure-of-merit, we can estimate the ptychographical performance of our kinoform from the above analysis of the STXM results. As a reference, we use the results previously obtained using conventional 3D laser lithography at near-IR wavelengths.[29] Considering the effects of the increased number of zones, the smaller effective outermost zone width, the slightly larger diameter, and the reduced focusing efficiency, we obtain an improvement in the figure-of-merit by a factor of about 1.6.

As a next step, we examined the performance of the kinoform through a ptychographic analysis. The results of the ptychographic reconstruction of the phase and amplitude images of the Siemens star test sample exhibit all of its features down to the central 30 nm spokes (see **Figure 6**a,b). The reconstructed pixel size of about 18.5 nm was determined from the distance between sample and CCD, the illumination wavelength, and the detection NA.[40] A simultaneously reconstructed complex illumination function was used to calculate the 3D wavefield along the optical axis using a free-space Fourier beam propagation method to reveal the distribution of intensity in the vicinity of the focal plane, as shown in Figure 6c. The amplitude of the wavefield at the circle of least confusion was derived from this 3D wavefield and is shown in Figure 6d. The overall size of the reconstructed spot is in good agreement with the STXM results. However, there seems to be a slight astigmatism in the spot (see Figure 6d), which can be attributed to the above mentioned nonconcentricity of the kinoform (see Figure 5d).

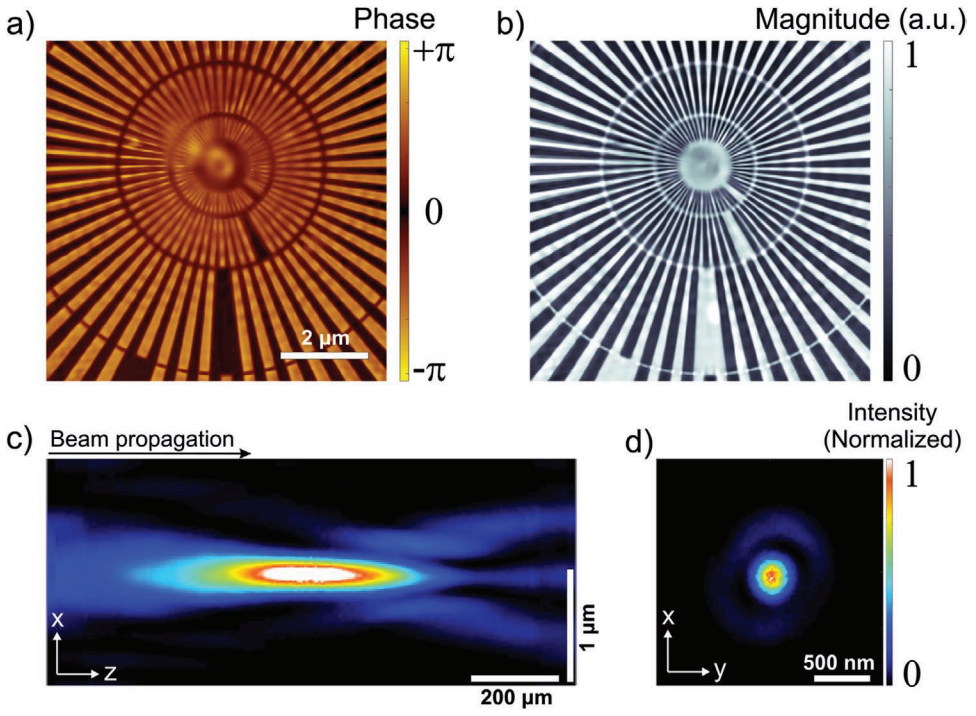

Figure 6. Ptychographic coherent diffractive imaging results. Ptychographic reconstruction of the a) phase and b) magnitude of the Siemens star test sample. The smallest inner features of the Siemens star, which have a size of 30 nm are resolved. c) The wavefield propagation of the intensity downstream of the kinoform showing the intensity distribution along the optical axis. A slight astigmatism is visible d) Amplitude of the reconstructed illumination function of the kinoform at the circle of least confusion.

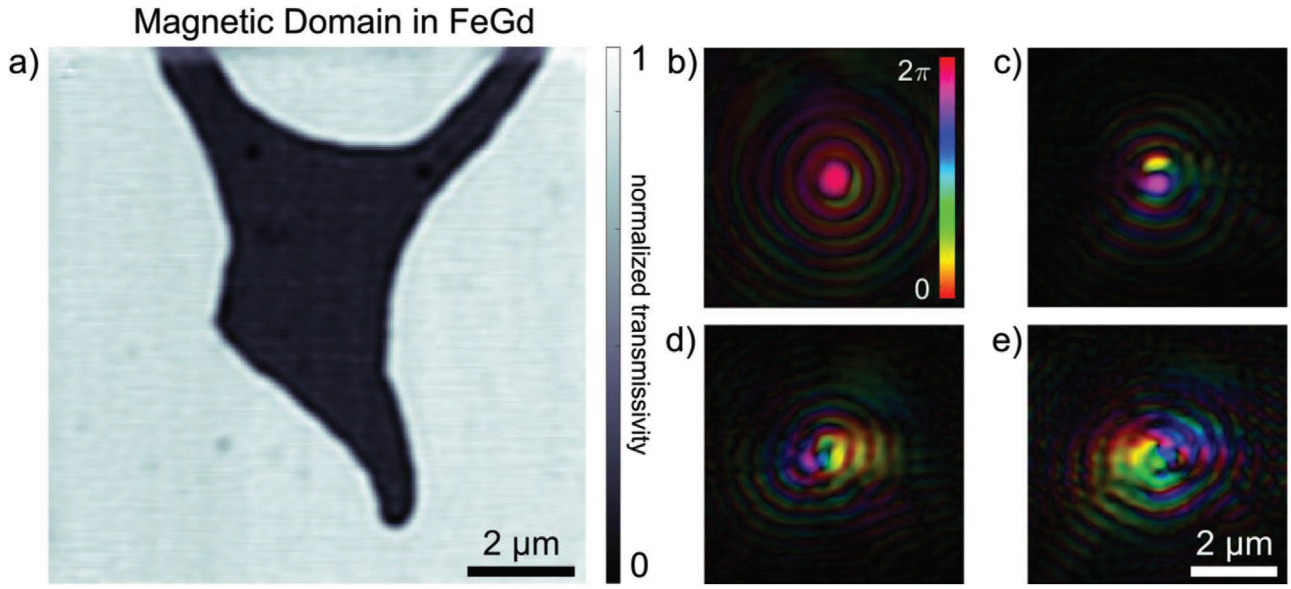

Figure 7. Ptychography of a FeGd thin film with out-of-plane (oop) magnetic domains using circularly polarized X-rays at an energy of 709 eV. a) Reconstructed complex object showing large domain structures at the Fe L_3-edge. Some fine-structure in the domains can be seen, which might be due to the sample itself or reconstruction artifacts. b–e) The most intense four modes in the complex illumination function. The fundamental mode (b) has 94% of the intensity. The precise origin of the higher-order modes would require further analysis. In all of the complex plots, the hue correlates with the phase and the brightness is proportional to the intensity.

To further demonstrate the potential of the optics in a more realistic use case, the 3D printed kinoforms were used to image the magnetization distribution of an amorphous iron-gadolinium (FeGd) magnetic multi-layer thin film with out-of-plane (oop) magnetization using X-ray circular magnetic dichroism (XMCD) contrast. The absorption contrast of 0.06 at the Fe L_3-edge is significantly smaller compared to the 180 nm thick gold lines of the Siemens star with a Michelson contrast of 0.91 at 709 eV. The reconstructed object can be seen in **Figure 7**a. From this multi-modal reconstruction, we also derived the mode decomposition in the illumination function.[41,42] The most intense top four modes are shown in Figure 7b–e. The purity of the fundamental mode was 94%. The slight decoherence can originate from source instabilities and higher modes or vibration of the sample or the optic.[44] However, considering that a purity of 95–100% would correspond to a fully coherent illumination, we can conclude that the kinoform performs well in filtering out the high harmonic contributions from the undulator, even in the absence of a beamstop.

3. Conclusions

In summary, 405 nm based 3D laser lithography was employed to 3D print kinoform X-ray holographic lenses with half the critical structure size compared to our previous work,[29] which used a wavelength of 780 nm. As a result, we have almost doubled the resolving power of the 3D printed lenses down to 145 nm half-pitch resolution as evidenced by STXM, Fourier ring correlation (FRC) analysis, and ptychographic reconstruction of the probe. A measured focusing efficiency of 7.6% at 700 eV photon energy was achieved, resulting in a 1.6-fold increase of the figure-of-merit for coherent imaging compared to the state-of-the-art. Furthermore, we demonstrated a realistic use case by imaging a low-contrast magnetic sample. The focusing efficiencies obtained here are larger than those previously obtained using gold kinoforms,[21] which were made by focused-ion-beam milling and operated at comparable photon energies.

The 3D printing manufacturing approach presented here can potentially be less expensive than other established approaches. Several future improvements are conceivable. For example, faster laser-focus scanning would reduce the effects of drifts during the printing process and enable finer discretization of the kinoforms, which is expected to reduce the surface roughness. Given the rapid progress in the field of 3D laser nanoprinting,[43] it can be expected that the efficiency as well as the resolving power of potentially inexpensive 3D printed kinoforms will improve further in the near future.

4. Experimental Section

Modeling of the Kinoforms: The kinoforms were modeled according to the usual set of parametric equations[36]

$$\begin{aligned} x &= r\cos(\theta) \\ y &= r\sin(\theta) \\ z &= t_{\max} \bmod((r/K)^2,1) \\ K &= A\sqrt{f/E} \end{aligned} \tag{3}$$

where $t_{\max}$ is the thickness, $0 \le r \le R$ the radius of the lens in µm, and $0 \le \theta \le 2\pi$ the azimuthal angle. The quantities R and t are the radius and the thickness of the kinoform, respectively. The factor K defines the radius of curvature of the lens and depends on a constant A, the focal length f, and the design energy E.

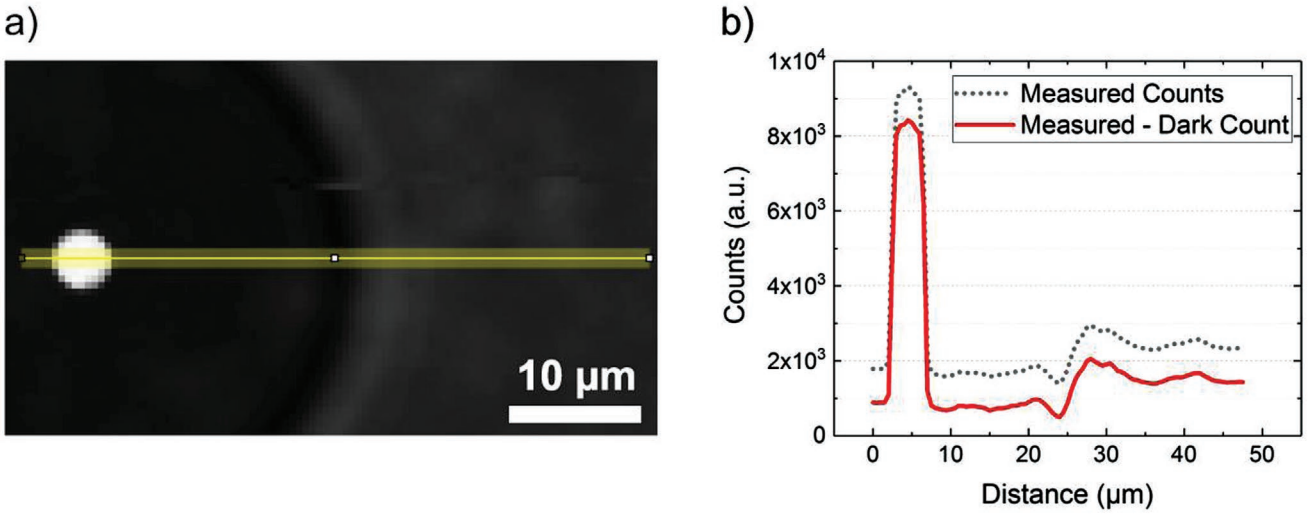

Figure 8. a) Image recorded by raster scanning a pinhole with a diameter of 4.4 µm at the focal distance of the focusing optic. The bright spot is a convolution of the focal spot and the pinhole. The black disc around the bright spot depicts the photon count coming through the kinoform's zones. The gray region on the right side of the image shows the incident count. b) Intensity profile along the yellow line in (a). The red curve corresponds to the corrected count after subtraction of the dark count of the APD.

The free 3D computer graphics software Blender and its XYZ Math Surface add-on were used to create a 3D model of the kinoforms according to these equations. As design parameters, an outermost period of $\Lambda - \sqrt{\Lambda^2 - K^2} = 400$ nm and a diameter of $2R = 40$ µm were chosen. The thickness was set to $t_{max} = 2$ µm resulting in an aspect ratio of 5 for the smallest features. The 3D model was then exported in the STL file format and converted to trajectories with the software DeScribe 2.5 (Nanoscribe GmbH) using a slicing and hatching distance of 100 nm. Finally, the trajectories were adapted to the MATLAB-based software of the 3D laser lithography setup.

Sample Preparation: The silicon nitride membranes (500 µm × 500 µm × 100 nm), which are embedded in silicon frames (5 mm × 5 mm × 100 µm), were purchased from Silson Ltd. (Warwickshire, U.K.). Prior to printing, the membranes were silanized for better adhesion of the structures: After activating the surface using an air plasma for 10 min, the substrates were placed in a solution of 3-(trimethoxysilyl)propyl methacrylate in toluene for 90 min and subsequently rinsed with deionized water.

3D Laser Lithography Setup: The home-built 3D laser lithography setup is based on a Ti:sapphire laser oscillator (Spectra Physics, MaiTai HP), which emited femtosecond laser pulses centered at a wavelength of 810 nm which are frequency-doubled in a SHG crystal resulting in a center wavelength of 405 nm. An acousto-optic modulator was used both as a high-frequency shutter and for gapless tuning of the excitation power. The pulses were tightly focused via a 100× oil-immersion objective (Leica HCX PL APO, NA = 1.4, 230 µm working distance). In order to move the sample with respect to the laser focus, a piezoelectric stage (PI P-527.3CL) was used.

The point spread function of the laser focus was measured by scanning a 80 nm gold nanoparticle and subsequently measuring the intensity of the backscattered light with a photodiode. Using 405 nm excitation center wavelength, a full width half maximum of the laser focus of ≈175 nm in lateral direction and 620 nm in axial direction was achieved. While the lateral resolution was in good agreement with corresponding theoretical calculations of the vectorial field distribution of the laser focus in photoresist, the axial resolution could be improved.

Laser Printing of the Kinoforms: The 3D laser-printing configuration was shown and discussed in Figure 1. In this configuration, the X-ray lenses were printed on top of the silanized Si_3N_4 membranes. Pentaerythritol triacrylate (PETA, Sigma Aldrich) was used as photoresist. The coverslips shown in Figure 1 have a thickness of 170 µm. The immersion oil was purchased from Leica Microsystems GmbH (Type F, $n = 1.5180$). An optimization of the writing parameters led to best results for a writing speed of 25 µm s^{-1} and a mean laser power of 1.5 mW as measured in the back focal plane of the objective lens. In the last step of the fabrication process, the samples were developed in mr-Dev 600 (micro resist technology GmbH) for 15 min, transferred to acetone, and dried using a supercritical drying process to avoid damage to the high aspect-ratio structures.

STXM Experiments: The soft X-rays with variable polarization in the energy range of 200–1800 eV were provided by an APPLE II type helical undulator. A grating monochromator was used to monochromatize the X-ray beam. A set of vertical and horizontal slits controlled the energy resolution and coherence. A kinoform located 3 m downstream the slits was used to focus the X-rays onto a sample, while an order selecting aperture filtered the undesired diffraction orders. The laser interferometrically controlled sample stage, that allows to move the sample in three axes with nanometer accuracy, was used for raster scanning the sample. An APD was used for STXM imaging.

The STXM imaging tests were performed using the third positive undulator harmonic. For imaging the linear test sample, a photon energy of 900 eV was used with exit slits set to 30 µm × 30 µm. The image acquisition time was 10 ms and a step size of 80 nm was used. For the Siemens star test sample a photon energy of 700 eV was used with exit slits set to 25 µm × 25 µm, 40 nm step size, and a 1.25 ms image acquisition time.

FRC was carried out using two subsequent images that were acquired with identical scanning parameters using the updated (July 2019) version of the FIJI FRC plug-in made by BIOPS.[45] The two images were aligned using the register plug-in of FIJI prior to FRC.

Efficiency Tests: For the diffraction efficiency estimations, a pinhole with a diameter of 4.4 µm was raster scanned in the first-order focal plane while simultaneously recording the incident intensity, projected zeroth order, and the first-order focal spot using an APD. The resulting image consisted of a convolution of the focusing optic and the 4.4 µm pinhole. An example is shown in **Figure 8**a. For calculating the diffraction efficiency, the dark count was measured and subtracted (see Figure 8b). Additionally, the absorption of the 100 nm thick SiN membrane was subtracted. Corresponding absorption data for each energy were obtained from the CXRO webpage.[46]

Ptychography: A charge-coupled device (pnCCD) designed specifically for X-ray detection was used to detect the far field diffraction pattern.[47] The CCD had 264 pixels with a size of 48 µm × 48 µm. The experiments were carried out at 900 eV with 15 µm × 15 µm exit slits

and 150 ms dwell time using the third undulator harmonic. The details of the upsampling method and mixed state analysis techniques used for the reconstructions shown in Figure 7 are explained in the literature.[48,49]

In ptychographic imaging, the achievable image resolution can be ultimately limited by the available coherent dose, as discussed in the text. However, when the resolution is not dose-limited (like in the authors' case) the reconstructed pixel size defines the resolution. The reconstructed pixel size is a function of the X-ray wavelength, the sample CCD distance, the number of pixels on the CCD, and the physical size of the CCD pixels. Physical limitations resulting from the mechanical design of the ptychography set-up were explained elsewhere.[50]

Fabrication of the FeGd Magnetic Sample: The ferromagnetic FeGd sample with out-of-plane (oop) magnetization under zero field was deposited using ion beam sputtering of 70 alternating layers of 3.6 Å thick Fe and Gd.

Acknowledgements

Authors thank Helmholtz Zentrum Berlin and BESSYII for beamtime allocation and B. Ludescher of MPI-IS for deposition of the FeGd sample. The KIT authors acknowledge funding by the Deutsche Forschungsgemeinschaft (DFG, German Research Foundation) under Germany's Excellence Strategy for the Excellence Cluster "3D Matter Made to Order" (EXC 2082/1–390761711), by the Carl Zeiss Foundation, by the Helmholtz program "Materials Systems Engineering," and by the Karlsruhe School of Optics and Photonics (KSOP). The authors thank Julian Köpfler (KIT) for helpful discussions and support in the early stages of the project.

Open access funding enabled and organized by Projekt DEAL.

Conflict of Interest

The authors declare no conflict of interest.

Author Contributions

U.T.S. and T.M. contributed equally to this work. C.K. and U.T.S. conceived the idea. U.T.S. and K.K. designed the optic. K.K. modeled the lens. T.M. and C.K. prepared the input files for the 3D laser lithography system. T.M. fabricated the lenses and conducted SEM imaging. U.T.S. and K.K. secured the beamtime allocation and performed the X-ray imaging, spectroscopy, and ptychography experiments. U.T.S. performed the data analysis. L.L. performed the ptychography reconstruction on magnetic sample data. M.W. (BESSY) provided beamline support. U.T.S., T.M., C.K., and K.K. wrote the initial manuscript draft. G.S. and M.W. (KIT) supervised the study. All authors contributed to the final manuscript.

Data Availability Statement

The data that support the findings of this study are available from the corresponding author upon reasonable request.

Keywords

3D laser lithography, kinoforms, multi-photon polymerization, X-ray microscopy, X-ray optics

Received: January 6, 2022
Published online: February 24, 2022

[1] B. Niemann, D. Rudolph, G. Schmahl, *Appl. Opt.* **1976**, *15*, 1883.
[2] P. Kirkpatrick, A. V. Baez, *J. Opt. Soc. Am.* **1948**, *38*, 766.
[3] G. Schmahl, D. Rudolph, P. Guttmann, O. Christ, in *X-Ray Microscopy* (Eds: G. Schmahl, D. Rudolph), Springer, Berlin, Heidelberg **1984**, pp. 63–74.
[4] J. Kirz, C. Jacobsen, *J. Phys.: Conf. Ser.* **2009**, *186*, 012001.
[5] B. Kepsutlu, V. Wycisk, K. Achazi, S. Kapishnikov, A. J. Pérez-Berná, P. Guttmann, A. Cossmer, E. Pereiro, H. Ewers, M. Ballauff, G. Schneider, J. G. McNally, *ACS Nano* **2020**, *14*, 2248.
[6] C. Hagen, K. C. Dent, T. Zeev-Ben-Mordehai, M. Grange, J. B. Bosse, C. Whittle, B. G. Klupp, C. A. Siebert, D. Vasishtan, F. J. Bäuerlein, J. Cheleski, S. Werner, P. Guttmann, S. Rehbein, K. Henzler, J. Demmerle, B. Adler, U. Koszinowski, L. Schermelleh, G. Schneider, L. W. Enquist, J. M. Plitzko, T. C. Mettenleiter, K. Grünewald, *Cell* **2015**, *163*, 1692.
[7] J. L. Fife, M. Rappaz, M. Pistone, T. Celcer, G. Mikuljan, M. Stampanoni, *J. Synchrotron Radiat.* **2012**, *19*, 352.
[8] M. Holt, R. Harder, R. Winarski, V. Rose, *Annu. Rev. Mater. Res.* **2013**, *43*, 183.
[9] A. Sakdinawat, D. Attwood, *Nat. Photonics* **2010**, *4*, 840.
[10] M. Yabashi, H. Tanaka, *Nat. Photonics* **2017**, *11*, 12.
[11] U. T. Sanli, C. Jiao, M. Baluktsian, C. Grévent, K. Hahn, Y. Wang, V. Srot, G. Richter, I. Bykova, M. Weigand, G. Schütz, K. Keskinbora, *Adv. Sci.* **2018**, *5*, 1800346.
[12] J. Vila-Comamala, S. Gorelick, E. Färm, C. M. Kewish, A. Diaz, R. Barrett, V. A. Guzenko, M. Ritala, C. David, *Opt. Express* **2011**, *19*, 175.
[13] W. Chao, P. Fischer, T. Tyliszczak, S. Rekawa, E. Anderson, P. Naulleau, *Opt. Express* **2012**, *20*, 9777.
[14] C. Chang, A. Sakdinawat, *Nat. Commun.* **2014**, *5*, 4243.
[15] K. Keskinbora, U. T. Sanli, M. Baluktsian, C. Grévent, M. Weigand, G. Schütz, *Beilstein J. Nanotechnol.* **2018**, *9*, 2049.
[16] K. Keskinbora, C. Grévent, U. Eigenthaler, M. Weigand, G. Schutz, *ACS Nano* **2013**, *7*, 9788.
[17] K. Keskinbora, U. T. Sanli, C. Grévent, G. Schütz, in *X-Ray Nanoimaging: Instruments and Methods II*, Vol. 9592, SPIE, Bellingham, WA **2015**, p. 95920H.
[18] D. Attwood, A. Sakdinawat, *X-Rays and Extreme Ultraviolet Radiation: Principles and Applications*, Cambridge University Press, Cambridge **2017**.
[19] D. A. Buralli, G. M. Morris, J. R. Rogers, *Appl. Opt.* **1989**, *28*, 976.
[20] L. Lesem, P. Hirsch, J. Jordan, *IBM J. Res. Dev.* **1969**, *13*, 150.
[21] K. Keskinbora, C. Grévent, M. Hirscher, M. Weigand, G. Schütz, *Adv. Opt. Mater.* **2015**, *3*, 792.
[22] A. Takeuchi, Y. Suzuki, K. Uesugi, I. Okada, H. Iriguchi, *Jpn. J. Appl. Phys.* **2012**, *51*, 022502.
[23] S. Tamura, M. Yasumoto, N. Kamijo, K. Uesugi, A. Takeuchi, Y. Terada, Y. Suzuki, *J. Phys.: Conf. Ser.* **2009**, *186*, 012075.
[24] E. D. Fabrizio, F. Romanato, M. Gentili, S. Cabrini, B. Kaulich, J. Susini, R. Barrett, *Nature* **1999**, *401*, 895.
[25] I. Mohacsi, P. Karvinen, I. Vartiainen, V. A. Guzenko, A. Somogyi, C. M. Kewish, P. Mercere, C. David, *J. Synchrotron Radiat.* **2014**, *21*, 497.
[26] J. Rodenburg, A. Maiden, in *Springer Handbook of Microscopy* (Eds: P. W. Hawkes, J. C. H. Spence), Springer, Cham **2019**, pp. 819–904.
[27] P. Thibault, M. Dierolf, A. Menzel, O. Bunk, C. David, F. Pfeiffer, *Science* **2008**, *321*, 379.
[28] A. Schropp, R. Hoppe, J. Patommel, D. Samberg, F. Seiboth, S. Stephan, G. Wellenreuther, G. Falkenberg, C. Schroer, *Appl. Phys. Lett.* **2012**, *100*, 253112.
[29] U. T. Sanli, H. Ceylan, I. Bykova, M. Weigand, M. Sitti, G. Schütz, K. Keskinbora, *Adv. Mater.* **2018**, *30*, 1802503.
[30] V. Hahn, P. Kiefer, T. Frenzel, J. Qu, E. Blasco, C. Barner-Kowollik, M. Wegener, *Adv. Funct. Mater.* **2020**, *30*, 1907795.
[31] J. Fischer, M. Wegener, *Laser Photonics Rev.* **2013**, *7*, 22.
[32] J. Fischer, M. Wegener, *Opt. Mater. Express* **2011**, *1*, 614.

[33] R. Wollhofen, J. Katzmann, C. Hrelescu, J. Jacak, T. A. Klar, *Opt. Express* **2013**, *21*, 10831.
[34] P. Mueller, M. Thiel, M. Wegener, *Opt. Lett.* **2014**, *39*, 6847.
[35] A. Wickberg, A. Abass, H.-H. Hsiao, C. Rockstuhl, M. Wegener, *Adv. Opt. Mater.* **2019**, *7*, 1801235.
[36] B. Morgan, C. M. Waits, J. Krizmanic, R. Ghodssi, *J. Microelectromech. Syst.* **2004**, *13*, 113.
[37] M. Weigand, Ph.D. Thesis, University of Stuttgart, Stuttgart **2015**.
[38] Y. Vladimirsky, D. Kern, T. H. P. Chang, D. Attwood, H. Ade, J. Kirz, I. McNulty, H. Rarback, D. Shu, *J. Vac. Sci. Technol., B: Microelectron. Nanometer Struct.–Process., Meas., Phenom.* **1988**, *6*, 311.
[39] C. A. Schneider, W. S. Rasband, K. W. Eliceiri, *Nat. Methods* **2012**, *9*, 671.
[40] J. W. Goodman, *Introduction to Fourier Optics*, Roberts and Company Publishers, Greenwood Village, CO **2005**.
[41] P. Thibault, A. Menzel, *Nature* **2013**, *494*, 68.
[42] L. Loetgering, M. Baluktsian, K. Keskinbora, R. Horstmeyer, T. Wilhein, G. Schütz, K. S. E. Eikema, S. Witte, *Sci. Adv.* **2020**, *6*, 7.
[43] V. Hahn, T. Messer, N. M. Bojanowski, E. R. Curticean, I. Wacker, R. R. Schröder, E. Blasco, M. Wegener, *Nat. Photonics* **2021**, *15*, 938.
[44] J. N. Clark, X. Huang, R. J. Harder, I. K. Robinson, *Phys. Rev. Lett.* **2014**, *112*, 113901.
[45] R. P. Nieuwenhuizen, K. A. Lidke, M. Bates, D. L. Puig, D. Grünwald, S. Stallinga, B. Rieger, *Nat. Methods* **2013**, *10*, 557.
[46] B. L. Henke, E. M. Gullikson, J. C. Davis, *At. Data Nucl. Data tables* **1993**, *54*, 2.
[47] I. Ordavo, S. Ihle, V. Arkadiev, O. Scharf, H. Soltau, A. Bjeoumikhov, S. Bjeoumikhova, G. Buzanich, R. Gubzhokov, A. Günther, *Nucl. Instrum. Methods Phys. Res., Sect. A* **2011**, *654*, 250.
[48] L. Loetgering, M. Rose, D. Treffer, I. A. Vartanyants, A. Rosenhahn, T. Wilhein, *Adv. Opt. Technol.* **2017**, *6*, 475.
[49] L. Lötgering, M. Rose, K. Keskinbora, M. Baluktsian, G. Dogan, U. Sanli, I. Bykova, M. Weigand, G. Schütz, T. Wilhein, *Opt. Eng.* **2018**, *57*, 084106.
[50] U. T. Sanli, *Ph.D. Thesis, University of Stuttgart*, Stuttgart **2019**.